

*Annual Review of Marine Science*Variations in Ocean Mixing
from Seconds to Years

James N. Moum

College of Earth, Ocean, and Atmospheric Sciences, Oregon State University, Corvallis,
Oregon 97330-5503, USA; email: jim.moum@oregonstate.edu

Annu. Rev. Mar. Sci. 2021. 13:201–26

First published as a Review in Advance on
June 29, 2020The *Annual Review of Marine Science* is online at
marine.annualreviews.org<https://doi.org/10.1146/annurev-marine-031920-122846>Copyright © 2021 by Annual Reviews.
All rights reserved**Keywords**

turbulence, mixing, temporal variability

Abstract

Over the past several decades, there has developed a community-wide appreciation for the importance of mixing at the smallest scales to geophysical fluid dynamics on all scales. This appreciation has spawned greater participation in the investigation of ocean mixing and new ways to measure it. These are welcome developments given the tremendous separation in scales between the basins, $\mathcal{O}(10^7)$ m, and the turbulence, $\mathcal{O}(10^{-2})$ m, and the fact that turbulence that leads to thermodynamically irreversible mixing in high-Reynolds-number geophysical flows varies by at least eight orders of magnitude in both space and time. In many cases, it is difficult to separate the dependencies because measurements are sparse, also in both space and time. Comprehensive shipboard turbulence profiling experiments supplemented by Doppler sonar current measurements provide detailed observations of the evolution of the vertical structure of upper-ocean turbulence on timescales of minutes to weeks. Recent technical developments now permit measurements of turbulence in the ocean, at least at a few locations, for extended periods. This review summarizes recent and classic results in the context of our expanding knowledge of the temporal variability of ocean mixing, beginning with a discussion of the timescales of the turbulence itself (seconds to minutes) and how turbulence-enhanced mixing varies over hours, days, tidal cycles, monsoons, seasons, and El Niño–Southern Oscillation timescales (years).

www.annualreviews.org

- Download figures
- Navigate cited references
- Keyword search
- Explore related articles
- Share via email or social media

1. INTRODUCTION

In seawater, velocity differences reduced to scales of millimeters to centimeters dissipate rapidly to heat (tens of seconds). Temperature and salinity, because they diffuse more slowly, are compressed to smaller scales, and thermal and haline differences diffuse somewhat less rapidly. It is the mechanical stirring of turbulence that acts to reduce length scales so that mixing by molecular diffusion proceeds efficiently. In the absence of turbulence sources, turbulence in the stratified ocean decays over a buoyancy period. That is, on the timescales of geophysical fluid dynamics, the turbulence itself decays rapidly.

On timescales of minutes to hours, various forms of fluid dynamical instability form, grow to finite amplitude, and break, renewing the turbulence. At a single point in space, the turbulence exhibits tremendous natural variability due to the multitude of processes that lead to turbulence and, finally, to mixing. The fact that the sequence of events leading from instability to mixing is not yet clear is a theoretical limitation (Smyth & Carpenter 2019). Our inability to make truly comprehensive measurements of turbulence in space and time is an observational limitation. However, we do have snapshots of these phenomena that provide guidance, toward parameterization, for example.

On timescales of days, the upper ocean is alternately heated, generally suppressing turbulence, and cooled, causing turbulence through convective instability. The details of how the ocean responds is critical to how heat is transported to the deep ocean, for example, and depends on local wind and wave forcing at the sea surface. Much has been learned about these processes through upper-ocean turbulence profiling experiments and by comparison with results from the atmospheric boundary layer.

Tidal forces introduce various pathways to mixing, including tidal friction in shallow waters and topographic interactions that cause hydraulic jumps over obstacles and create an internal tide over continental shelves that evolves into a highly nonlinear, strongly mixing internal wave field that modifies the stratification over the shelves. On roughly similar timescales, near-inertial internal gravity waves are generally a response to wind forcing that propagate (usually downward) and create thin layers of high shear where turbulence occurs.

Recent long time series of measurements of turbulence on moored platforms have revealed how ocean mixing varies in response to westerly wind bursts of the Madden–Julian Oscillation, monsoons, seasonal heating, and variations in the El Niño–Southern Oscillation, where in each case we discover that mixing matters.

While these examples represent a broad range of timescales, results have been gleaned from relatively few experiments and time series at a few locations. It is hoped that the discussion and references herein help to summarize the present state of our knowledge of ocean mixing timescales and, more importantly, help the reader to define future targets of investigation. Results that show timescales increasing from seconds to years are presented sequentially. Included are a discussion intended to promote confidence in our ability to make measurements of turbulence in the ocean so as to quantify these measurements in a useful manner (Section 3) and one that shows where prolonged absences of turbulence in the ocean have been found (Section 5).

2. TIMESCALES OF TURBULENCE

Thermodynamic changes to a fluid parcel are achieved by diffusive mixing at molecular scales. In a laminar fluid, this process is slow. Turbulence (or mechanical stirring) acts to increase concentration gradients, thereby enhancing mixing across them. These increased concentration gradients present a microstructure of fluid properties, such as temperature. In the ocean science community, the terms mixing, turbulence, and microstructure are sometimes used interchangeably, but the distinctions ought to be clear.

Thermodynamic changes to a fluid parcel are achieved only by mixing. Turbulence (as quantified by an energy dissipation rate) and turbulence-enhanced mixing (as estimated through use of a turbulence diffusivity) vary by at least eight orders of magnitude in the ocean in both space and time. This is a statement of the tremendous natural variability of geophysical turbulence with a high Reynolds number (Re). Re relates inertial to viscous forces, a ratio of a velocity scale times a length scale to fluid viscosity. High values mean that inertial forces dominate at large scales. Regardless, viscous forces are critical to the turbulence. In geophysical fluids in motion, Re is large because the length scales are large; by contrast, in aerodynamic flows, Re is large because the velocities are large. High Re in geophysical flows therefore refers to the vast range of length scales that must be resolved for a complete accounting of the fluid dynamics.

2.1. Diffusive Timescales

The smallest length scales of the turbulence are defined dimensionally in terms of the viscous rate of dissipation of turbulence kinetic energy, ϵ ; the corresponding mass and thermal diffusivities; and the corresponding viscosity (originally defined by Kolmogorov and Batchelor, but for a synopsis, see, for example, Pope 2000). The diffusivities and viscosity are physical properties of the media (in our case, seawater) and are defined by constitutive relations as the ratio of the flux of mass, heat, and momentum to the respective spatial gradient in the fluid (Bird et al. 2007). Fick's law of diffusion defines the diffusion coefficient for salt in seawater via $J_s = -D_s \partial_{x_i} S$, where J_s is the salt flux through the principal gradient of S and ∂_{x_i} represents differentiation with respect to the direction of the principal gradient, x_i . Similarly, the thermal diffusivity, γ , is defined by Fourier's law of thermal conduction $J_q = -\gamma \partial_{x_i} \theta$, and for a Newtonian fluid, the viscosity, ν , is defined by $\hat{\tau} = \nu \rho \partial_{x_i} \hat{u}$. Here, J_q and $\hat{\tau}$ are fluxes of heat and momentum, θ is temperature, ρ is density, and \hat{u} is velocity. These quantities and their dependencies on θ and pressure are empirically determined in the laboratory and are well known and repeatable. In the ocean, the smallest length scales are (a) the Kolmogorov length scale, which defines the smallest scales of motion, $\eta = (\nu^3/\epsilon)^{1/4}$; (b) the Batchelor length scale that defines the smallest scales of θ , $\eta_\theta = (\nu \gamma^2/\epsilon)^{1/4}$; and (c) the Batchelor length scale that defines the smallest scales of S , $\eta_s = (\nu D_s^2/\epsilon)^{1/4}$. Typical values of ν , γ , and D_s in seawater are 1.2×10^{-6} , 1.4×10^{-7} , and $1.4 \times 10^{-9} \text{ m}^2 \text{ s}^{-1}$, respectively. For reference, two values of η (1 mm and 5 mm) are shown in **Figure 1**. For the same values of ϵ , η_θ is smaller by a factor of \sqrt{Pr} , where the Prandtl number, Pr , is equal to ν/γ , and η_s is smaller by a factor of \sqrt{Sc} , where the Schmidt number, Sc , is equal to ν/D_s .

These fluid properties appear in their respective evolution equations as flux divergences. For example, the contribution of thermal diffusion to changing θ is represented as

$$\partial_t \theta = \partial_{x_i} (\gamma \partial_{x_i} \theta), \quad 1.$$

and since γ is nearly constant,

$$\partial_t \theta = \gamma \partial_{x_i}^2 \theta. \quad 2.$$

Here, ∂_t represents differentiation with respect to time, t . Scaling Equation 1 with timescale T and length scale L yields a length-scale-dependent diffusive timescale $T_\gamma = L^2/\gamma$. Similarly, T_ν is equal to L^2/ν , and T_s is equal to L^2/D_s . At the Kolmogorov and Batchelor length scales typical of ocean turbulence (on the order of millimeters to centimeters), diffusion proceeds rapidly (seconds to hundreds of seconds), as indicated in **Figure 1a**. The fact that molecular diffusion alone is ineffective at smoothing larger scales (more than a few centimeters) is also indicated in **Figure 1a**.

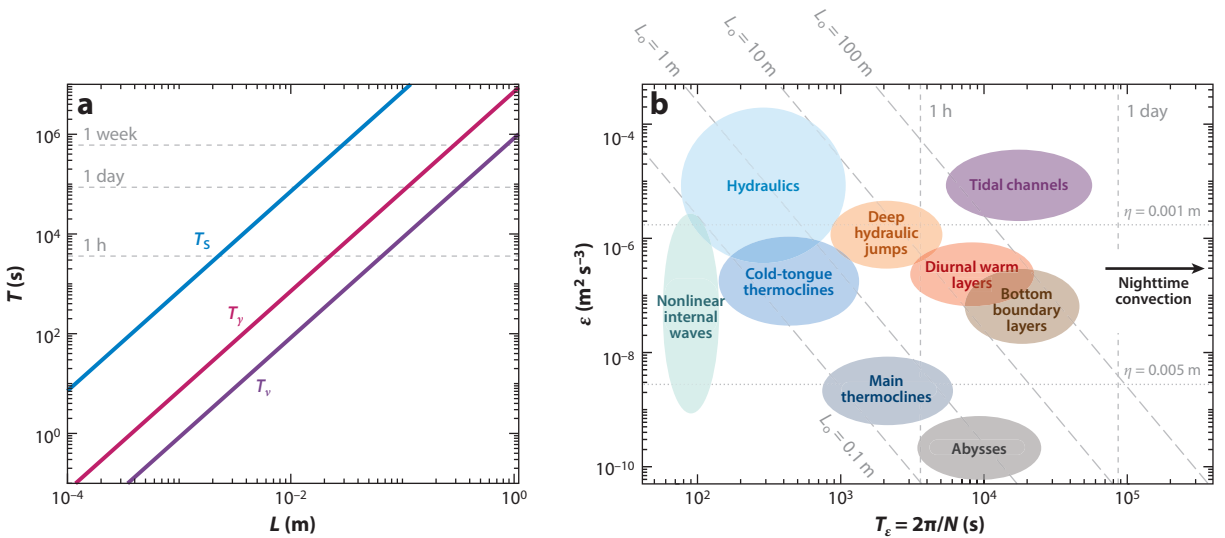


Figure 1

Time and length scales of turbulence in the ocean. (a) Diffusive timescales for salinity (T_s), temperature (T_y), and momentum (T_v) in turbulent flows over a range of length scales (L). (b) Decay timescale ($T_\epsilon = 2\pi/N$) versus ϵ . Dotted horizontal lines represent two values of the Kolmogorov scale, η . Dashed lines sloping up to the left represent constant values of the Ozmidov scale, L_o . The ovals indicate ranges for several observed oceanic phenomena: nonlinear internal waves (Moum et al. 2003), hydraulics (Wesson & Gregg 1994, Nash & Moum 2001, Klymak & Gregg 2004), cold-tongue thermoclines (Peters et al. 1995, Moum et al. 2009), main thermoclines (Moum & Osborn 1986, Moum 1996), abysses (Toole et al. 1994, Moum et al. 2002), deep hydraulic jumps (Polzin et al. 1996), diurnal warm layers (Sutherland et al. 2016, Moulin et al. 2018), bottom boundary layers (Perlin et al. 2005), tidal channels (Gargett 1994), and nighttime convection (Shay & Gregg 1986, Anis & Moum 1994).

It is the stirring motion induced by the turbulence that increases concentration gradients so that mixing at molecular scales is efficient. Alternatively, we might say that the turbulence reduces the length scales of the gradients to a size where diffusion proceeds rapidly. The evolution equations are complete without parameterization of the turbulence since turbulence evolves from the nonlinear advective terms (Pope 2000). Direct numerical simulations that completely solve the evolution equations develop fully three-dimensional turbulent flow fields (for example, Taylor et al. 2019, Smyth et al. 2001). While direct numerical simulation studies are helpful in understanding some aspects of ocean mixing, limited computational domains restrict the largest scales to a few meters at best, with periodic boundaries preventing proper evolution or relaxation of the turbulence. This limit to the range of computed scales also means that the full hierarchy of (sometimes interacting) instabilities that break geophysical flows down to the scales of turbulence is not included.

At the scales of geophysical fluid dynamics, the consequence of limited computational domains is that the resolution of geophysical scales precludes resolved turbulence in numerical solutions. An accommodation is to directly represent the turbulence in the evolution equations. This is commonly done in terms of a turbulence diffusivity (K_T) or viscosity (K_m), so that

$$\partial_t \theta = \partial_{x_i} [(K_T + \gamma) \partial_{x_i} \theta]. \quad 3.$$

While γ is a property of the fluid and nearly constant, K_T is a property of the flow and varies by orders of magnitude. Hence,

$$\partial_{x_i} [(K_T + \gamma) \partial_{x_i} \theta] \neq (K_T + \gamma) \partial_{x_i}^2 \theta. \quad 4.$$

DISSIPATIVE HEATING

We have said that ϵ is an energy sink. Since that energy is lost to heat, ϵ must contribute a source term in the evolution equation for heat. In a one-dimensional sense, this can be written as

$$\rho C_p \partial_t \theta = \partial_z J_q + \rho \epsilon$$

so that it can be compared in magnitude to either the heating rate θ_t or, by vertical integration, to the turbulent heat flux J_q . Dissipative heating contributes to tropical cyclone dynamics (Bister & Emanuel 1998) via the intense turbulence in the atmosphere's boundary layer, increasing wind speeds in tropical cyclones by perhaps 20%. If dissipative heating contributes significantly in the ocean, it must be immediately below the surface during wave breaking where and when the greatest values of ϵ in the ocean are observed (for example, Sutherland & Melville 2015). Indeed, Sinnet & Feddersen (2018) estimate, from measurements of surface wave flux divergence in the surf zone, that dissipative heating contributes tens of watts per square meter, comparable to the contribution above the sea surface in tropical cyclones. It is possible that it may also be a contributor beneath the sea surface in as yet unmeasured extreme storms, such as tropical cyclones.

2.2. Decay Timescale

Turbulence is a dissipative process. In the absence of forcing, the kinetic energy associated with the turbulence decays directly via ϵ to viscous heating (Pope 2000) (see the sidebar titled Dissipative Heating). In an unstratified fluid, the turbulence decays according to a time-dependent power law such that $\epsilon \propto t^n$, where $n \simeq -2$, a dependency that is apparently independent of Re (Sinhuber et al. 2015). From upper-ocean turbulence measurements through numerous squalls that acted to isolate subsurface turbulence from surface forcing by the density stratification produced by rainfall, Smyth et al. (1997) showed that the decay rate of turbulence in a stratified fluid is much faster. It is exponential—that is, $\epsilon \propto \exp(-t/T_\epsilon)$, where $T_\epsilon \simeq 2\pi/N$ and $N = \sqrt{-g/\rho \cdot \partial_z \rho}$ (see also Brainerd & Gregg 1993).

The decay timescale, T_ϵ , and ϵ are related through the Ozmidov or buoyancy length scale, $L_o = (\epsilon/N^3)^{1/2}$, which approximates the largest scales of isotropic turbulence in a stratified fluid. Flow structures with length scales greater than L_o are preferentially attenuated in their vertical dimension (Gargett et al. 1984). The fact that anisotropic turbulence persists at much larger horizontal than vertical size and scales spectrally with the same value of ϵ is potentially useful, but the phenomenon is still poorly understood (Lindborg 2006, Kunze 2019).

A rough sorting of ocean turbulence regimes follows from a comparison of T_ϵ and ϵ (**Figure 1b**). Turbulence that decays over periods longer than a few hours is rare and is typically influenced by other factors, such as proximity to a boundary (solid or free). This applies to the tidal channel, bottom boundary, and diurnal warm layers. In the case of nighttime convection, where the mixed-layer value of $N \rightarrow 0$, the forcing (the surface buoyancy flux) changes sign from a sink of turbulence energy to a source of turbulence energy over a few hours, and T_ϵ is not representative of the actual decay time.

One upshot of the discussion so far is that the title of this article is potentially misleading. Ocean mixing events are short lived (seconds to tens of minutes; **Figure 1**). Turbulence that continues on timescales much longer than this is a result of persistent instability of the larger-scale flow.

3. CONFIDENCE IN OCEAN MIXING MEASUREMENTS

An important issue in any discussion that attempts to quantify mixing's role in geophysical fluid dynamics or climate is the quality of the quantification. Signals derived from measurements of

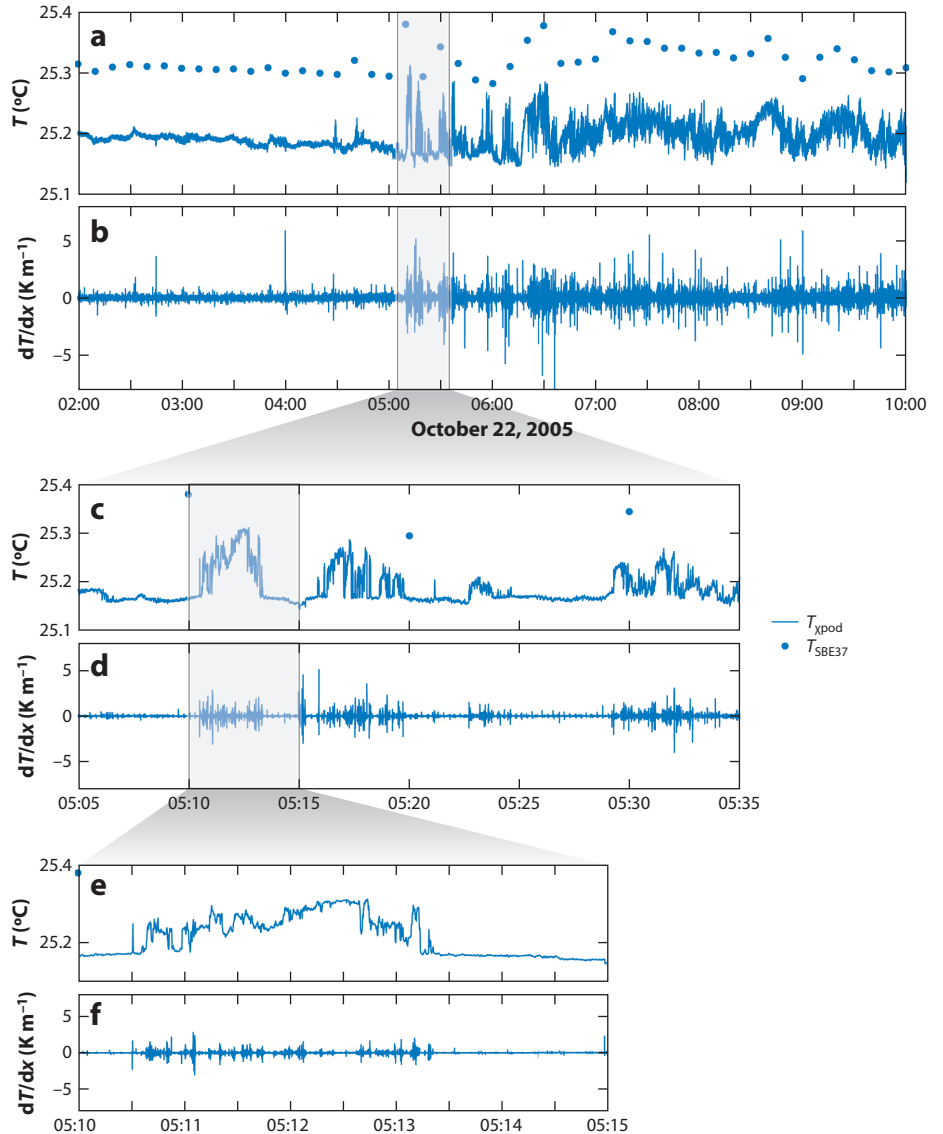


Figure 2

(a) Eight-hour records of temperature measured at 28-m depth and 10-min intervals from a Sea-Bird Scientific SBE 37 temperature sensor (blue dots) and near 29-m depth sampled at 100 Hz from the upper thermistor of a χ pod (blue line) located on an oceanographic mooring at $0^\circ, 140^\circ\text{W}$. (b) Temperature gradient dT/dx from the χ pod. (c,d) Expanded plots of the shaded regions in panels *a* and *b*, respectively. (e,f) Expanded plots of the shaded regions in panels *c* and *d*, respectively. The current speeds were $0.35\text{--}0.4\text{ m s}^{-1}$. Figure adapted with permission from Moum & Nash (2009).

high- Re turbulence are messy (**Figure 2**). Yet, despite the difficulties in understanding the details of turbulent flows (Pomeau 2016), quantitative assessments from in situ measurements of the effects of mixing on high- Re geophysical flows have proven to be reliable. This is in large part due to the universality of both kinetic energy and scalar spectra (or structure functions)

of the turbulence, thus permitting estimates of ϵ and χ (an analogous quantity to ϵ that represents the diffusive rate of dissipation of scalar variance—in ocean studies, typically temperature variance as measured using fast thermistors) by integration over all wavenumbers/frequencies or scaling over limited wavenumber/frequency ranges of the relevant spectra. Sensors to make these measurements have been deployed on a wide range of platforms (Lueck et al. 2002, Moum 2015), most recently including commercial gliders (Rainville et al. 2017, Schultze et al. 2017, St. Laurent & Merrifield 2017, Evans et al. 2018), Lagrangian floats (D'Asaro & Lien 2000), profiling floats (Shroyer et al. 2016), and oceanographic moorings using what we have been calling χ pods (Moum & Nash 2009), which are moored mixing meters outfitted with fast thermistors to sense temperature, a pitot-static tube to sense velocity, a compass, and pressure and acceleration sensors. Notably, such moored measurements that produce long time series of turbulence are not possible in the atmosphere outside of towers in the lowest few percent of the terrestrial boundary layer and immediately above the sea surface in the marine boundary layer. Sensing technology has reached a point of maturity where there is now rapidly developing interest in including turbulence sensors on operational profiling Argo floats (Roemmich et al. 2019).

We need to have confidence not only in the measurements but also in the inferences we make from them. Turbulence diffusivities are inferred from the insights of Osborn & Cox (1972) and Osborn (1980), which have provided the basis of our interpretations for more than 40 years. Assumptions and uncertainties have been recently reviewed by Gregg et al. (2018).

There are several good reasons why we should have confidence in the quantitative inferences that have been made from ocean turbulence measurements. The first is repeatability. Under the appropriate conditions (relatively low winds, deep enough preexisting thermoclines), nighttime convection creates a mixed layer in which $\epsilon \simeq (0.6–0.8)J_b^0$, where J_b^0 represents the surface buoyancy flux (Shay & Gregg 1986). This mixed layer is typically found beneath a surface layer forced primarily by the wind. This result is identical to that found in the boundary layer over land, when daytime buoyancy forcing drives convection. Similarity scaling of the convectively driven aquatic boundary layer has been repeatedly observed by Imberger (1985), Brubaker (1987), and Anis & Moum (1994) using similar but not identical measurement systems.

A second reason for confidence is interplatform comparisons. A three-and-a-half-day overlapping turbulence profiling sequence by two groups at the equator, each using independently developed sensors, platforms, and processing software, showed systematic bias in averaged profiles of ϵ of less than a factor of two, which in turn is less than conservative estimates of the cumulative uncertainties in the independent estimates of ϵ (Moum et al. 1995). Comparisons between profiling estimates of ϵ made from shear probes and moored estimates derived from fast thermistors have yielded similar results (Perlin & Moum 2012, Pujiana et al. 2018), with the estimates converging with increased averaging times to reduce the effects of the natural time and space variability of turbulence between platforms.

A third reason for confidence is that upper-ocean profiles of heat and momentum fluxes derived from in situ measurements converge to independently measured surface values of heat and momentum flux (Moum & Rippeth 2009, Pujiana et al. 2018), as indicated in **Figure 3**. The subsurface flux estimates both asymptote and covary with surface fluxes, estimated in this case from ship-based eddy-correlation techniques (DeSzeke et al. 2015).

Finally, integral estimates of mixing derived from tracer dyes injected at an isopycnal and tracked for periods of years have consistently yielded estimates of turbulence diffusivity that are within a factor of two of local microstructure estimates (Ledwell et al. 1998, 2000, 2004, 2011), as recently summarized by Gregg et al. (2018). The exception to this agreement, where turbulence measurements downstream of Drake Passage were an order of magnitude smaller than those inferred by tracer diffusion, was reconciled with a numerical simulation of the flow that suggested

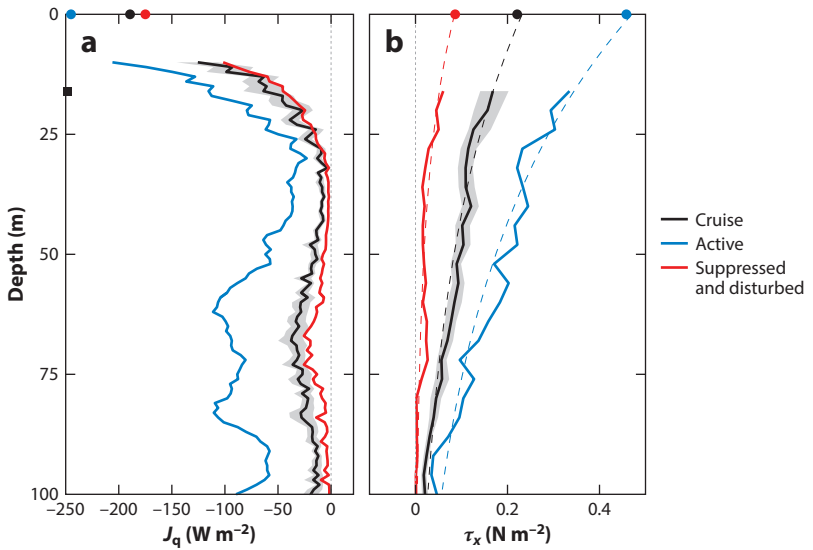


Figure 3

Vertical profiles of turbulence fluxes of (a) heat and (b) zonal (x -component) momentum, as assessed from turbulence profiling. In the legend, active refers to strong surface forcing, suppressed refers to weak surface forcing, and cruise includes data from the entire experiment. Surface values of the fluxes are indicated by the dots at a depth of 0 m. Measurements are from the equatorial Indian Ocean before (red) and during (blue) the passage of westerly wind bursts of the Madden–Julian Oscillation. Subsurface fluxes covary with the forcing and asymptote to surface values, as they must. Figure adapted with permission from Pujiana et al. (2018).

that the tracer was not mixed where the turbulence measurements were made but was instead advected across topographic features and subjected to intense mixing there before being advected back to the site of the turbulence measurements (Mashayek et al. 2017).

4. TEMPORAL VARIABILITY OF MIXING

During the early stages of interpreting signals from measurements of the microstructures of temperature and velocity, entire papers were devoted to understanding very limited data sets, in some cases just a few vertical profiles (Grant et al. 1962, Osborn 1974, Gregg 1977, Dillon & Caldwell 1980). However, the lessons learned from these interpretations led to more intensive observational strategies. The information content from rapidly profiling upper-ocean turbulence platforms deployed from ships for periods of up to a month or so yields detailed vertical profiles of the upper few hundred meters at roughly 10-min intervals. This enhancement in information content has led to improved understanding of a range of phenomena over those timescales. But while these analyses provide a close look at the vertical structure of the signatures of the turbulence, they provide no information either on the short-timescale variations of the turbulence or on any phenomena longer than can be resolved in a shipboard survey. An exception would be dye release experiments, which provide an integral of the mixing over longer periods but have the shortcoming that they do not reveal mechanisms. Sacrificing vertical resolution for detailed and extended time series at fixed depths on oceanographic moorings has led to new observations (Moum & Nash 2009) of both the details of local instabilities and how mixing varies on timescales longer than a shipboard campaign.

4.1. Minutes to Hours

A simple, albeit highly resolved, point temperature measurement from 29-m depth on an oceanographic mooring at the equator in the Pacific's cold tongue provides some insight into the short-timescale variations associated with turbulent overturns in this highly stratified flow and highlights the information not available to the typical 10-min sampling on these equatorial moorings (**Figure 2**). In this example, the turbulence is advected by the mean flow. In fact, the measurement requires advection past the sensor, as otherwise we would simply measure the wake turbulence of the sensor induced by vertical motion as the surface buoy is pumped by surface waves. Here, all data with horizontal flow speeds of less than 0.05 m s^{-1} are flagged and excluded from the analysis. In **Figure 2a,b**, there is a transition from cooler to warmer fluid coincident with a transition from less turbulent to more turbulent fluid, as indicated by the high-frequency part of the temperature signal dT/dx , defined here. (In practice, T is differentiated in time using electronic circuitry and converted to spatial gradient $dT/dx = \frac{1}{u}dT/dt$, where u is the flow speed past the sensor.) Closer examination (over 30 min in **Figure 2c,d** and 5 min in **Figure 2e,f**) indicates that the transition is intermittent. Relatively warm and turbulent fluid parcels suggest that they have been mixed downward by turbulence at shallower depth. The repeated structures in both T and dT/dx are suggestive of a fractal nature of the fluctuations (Sreenivasan 1991), although it is still not clear how to use fractal predictions for practical purposes in geophysical flows.

When stratified shear flows that are near marginal instability (that is, the Richardson number $Ri = N^2/Sh^2$ is persistently near 1/4, where Sh is the vertical gradient of current speeds) become unstable, wavelike features form, grow, and break, thereby creating turbulence. The characteristic billows of Kelvin–Helmholtz instability are visually revealed by clouds in the atmosphere (Smyth & Moum 2012), by filming in the laboratory (Thorpe 1971), and by divers in the ocean using short-timescale dye releases (Woods 1968) and have been detected in the ocean acoustically (Moum et al. 2003, Geyer et al. 2010, Chang et al. 2016) and by arrays of closely spaced, rapidly sampled temperature sensors (van Haren & Gostiaux 2010). The moored measurement shown in **Figure 2** leads, through averaging in different ways—here including estimating ϵ and computing a spectrogram—to a view that shows the semiregular pulsing of shear instabilities on longer timescales in **Figure 4**. This 52-day record was obtained in the South Equatorial Current, which, at the equator and 140°W , is almost always near marginal instability (Smyth & Moum 2013). The variance-preserving form of the spectrogram of temperature (**Figure 4a**) displays pulses at a frequency near 10^{-3} Hz (roughly 15 min), close to the timescales of both buoyancy, $2\pi/N$, and shear, $2\pi/Sh$. These pulses are the spectral signature of narrowband waves whose wavelength, phase speed, and vertical phase structure are consistent with our theoretical understanding of Kelvin–Helmholtz instability (Moum et al. 2011). The spectrogram in **Figure 4a** shows that periods of particularly high spectral amplitudes at the Kelvin–Helmholtz peak are often associated with a broadband elevation of the spectrum due to associated turbulence. The magnitude of ϵ at the depth of the sensor (**Figure 4c**) varies on a diurnal timescale but is also modulated on the timescales of the Kelvin–Helmholtz waves, as indicated by an estimate of the wave potential energy (**Figure 4b**), to which it is highly correlated (Moum et al. 2011). The dissipative timescale of the waves, as estimated by the ratio of the wave potential energy to ϵ , is $\mathcal{O}(10)$ oscillations, suggesting rapid decay. Indeed, this is consistent with the temporal patchiness of the spectral peaks in **Figure 4a**. Linear stability analysis using observed current and density profiles predicts the phase speed (c) and wavelength (λ), and hence the equivalent frequency $f_{KH} = c/\lambda$, of the fastest-growing instabilities. The mode of the histogram of f_{KH} computed for the time period shown is identical to the peak of the averaged variance-preserving spectrum (**Figure 4d**). A probabilistic theory of random instabilities predicts this peak frequency closely (Smyth et al. 2011) and suggests that it must

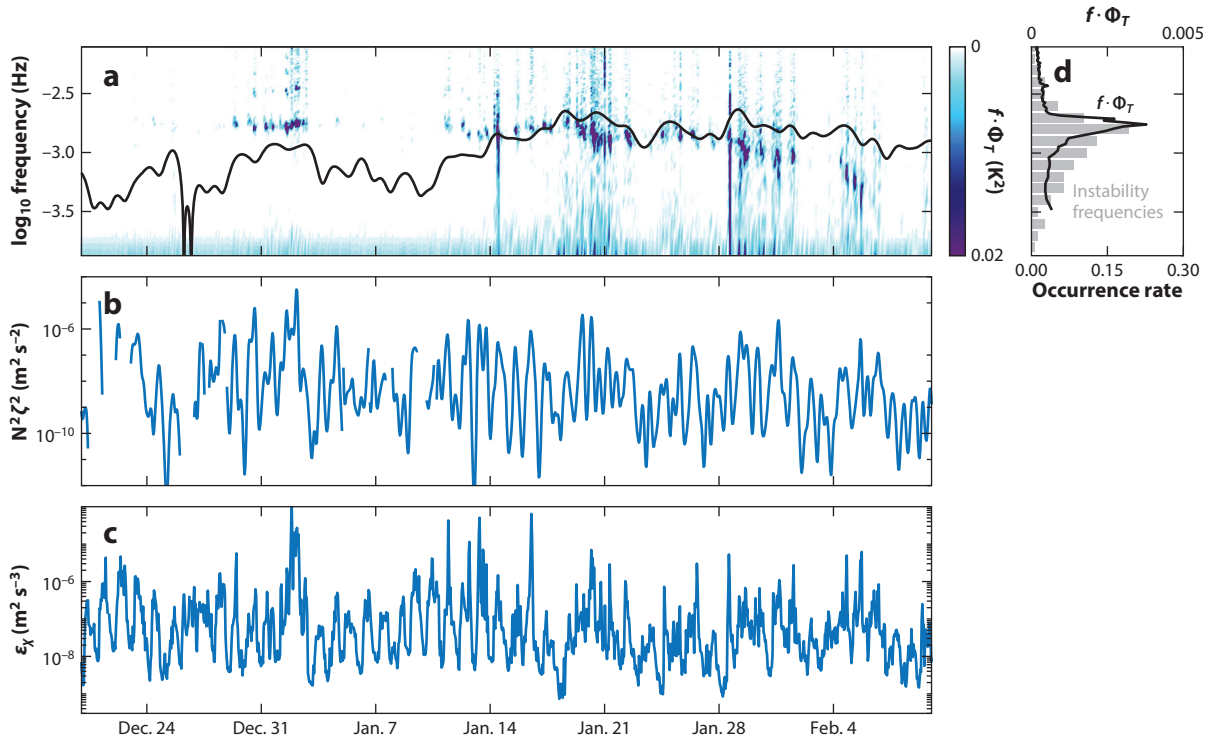


Figure 4

(a) Variance-preserving temperature spectrogram. The black line shows the local value of N . (b) $N^2 \xi^2$, a measure of potential energy variance due to near- N waves, where ξ is the near- N isothermal displacement. (c) ϵ at 29 m for a two-month period at $0^\circ, 140^\circ\text{W}$. (d) Histogram corresponding to frequencies estimated from 155 unstable modes, as determined from linear stability analysis applied to observed profiles of currents and stratification. The black line is the temperature spectrum (variance-preserving form) for the full period shown in panel a. Figure adapted with permission from Moum et al. (2011).

be roughly $N/2\pi$, a result that follows from the balance of shear and stratification that governs shear instability in geophysical flows.

These limited examples extracted from the unique perspective of continuous time series provide an indication of the details of the turbulence missed between successive profiles, for example. They permit the type of analysis that leads to a distinction between the various forms that a daily mixing cycle can take over long periods, seen in **Figure 4a** as the pulsing of nearly unstable Kelvin-Helmholtz waves in a marginally stable flow.

4.2. Daily

The upper ocean typically exhibits both a nighttime and a daytime peak in turbulence. These peaks are driven by the solar heating cycle and modulated by variations in surface wind stress. At night, the absence of solar heating leaves net surface heat fluxes that cool the sea surface. As a result, negatively buoyant fluid parcels build to a state where their net mass exceeds frictional forces, and these fluid parcels sink as convective plumes. If the preexisting thermocline is sufficiently deep (or weak), then only convection contributes to the turbulence in a mixed layer formed beneath a surface layer dominated by wind- and wind-wave-driven turbulence. The intermittent formation and subsequent sinking of convective plumes leads to an averaged potential temperature profile

that is superadiabatic—that is, the potential temperature increases downward from the sea surface (Anis & Moum 1992). The cooling surface heat flux contributes to a surface buoyancy flux that has the sign of a source term in the turbulent kinetic energy equation. In the mixed layer, ϵ is nearly equal to the surface buoyancy flux (Shay & Gregg 1986), an important result partly because, as stated in Section 3, it is one of the few simply repeatable results in high- Re geophysical turbulence.

This result followed from studies of atmospheric turbulence in the daytime boundary layer over land where heated (positively buoyant) plumes form at the surface, rise, and create a mixed layer above a surface layer driven by the shear created as the geostrophic wind decreases to zero at the surface. Although some details differ between nighttime convection in the ocean and daytime convection in the atmosphere over land, similarity scalings have proved useful in predicting aspects of the turbulence (Wyngaard et al. 1971) and show how these two fundamental geophysical examples of convection mirror each other in physical structure and dynamics.

The daytime peak in turbulence has been observed only recently (Sutherland et al. 2016), largely because of the difficulty in making clean measurements very near to the sea surface. These initial measurements were made with an autonomous and ascending turbulence profiler (ten Doeschate et al. 2017), permitting measurements through the sea surface undisturbed by ship wake. Subsequent measurements using towed sensors suspended from the bow of a ship (Moulin et al. 2018) and from a surface-following device towed behind the ship at roughly 45° outboard (Hughes et al. 2020) have expanded on this initial study.

The presence of turbulence-enhanced mixing had been anticipated in the diurnal warm-layer scalings of Price et al. (1986) and Fairall et al. (1996). When winds are sufficiently weak—less than approximately 8 m s⁻¹, in the case of the tropics (Thompson et al. 2019)—and the skies are sufficiently clear, the onset of penetrating solar radiation, which acts to stratify the upper meter or so even before the change in sign of net surface flux from cooling to heating, quickly isolates the subsurface ocean from surface forcing, and hence the subsurface turbulence begins to decay (Moulin et al. 2018). Because most of the solar radiation is absorbed in the upper meter or so, this layer can heat, by up to 3 K. If the wind speed exceeds approximately 2 m s⁻¹, the energy input by the wind is large enough relative to the buoyancy input by the sun to accelerate a surface jet sufficiently strong to induce marginal instability (Hughes et al. 2020). Turbulence ensues, thereby mixing the diurnal warm layer and jet downward, as shown in **Figure 5**. Because the diurnal jet veers inertially (to the right in the Northern Hemisphere and the left in Southern Hemisphere; Hughes et al. 2020), the direction of net transport of fluid in the diurnal warm layer differs from that in the mixed layer below, a factor not included in circulation models that do not resolve the diurnal warm layer. The diurnal warm layer is ultimately mixed by the following night's buoyancy forcing.

There is evidence that the diurnal warm layer feeds back to the boundary layer in the atmosphere, forcing convection there after sea surface temperature (SST) increases in late afternoon, supported by observations of increased precipitation and wind gustiness following peak SST (Ruppert & Johnson 2016). This convection is weaker than that in the boundary layer over land but appears to follow the same similarity scaling of ϵ (S.P. DeSzeoke, personal communication).

The descending shear layer in **Figure 5** is similar in timing and form to that shown in **Figure 6**, although the vertical scales are larger in **Figure 6**, the mean descent rates differ by a factor of three (as noted in the Figure captions), and in the latter case, the turbulence persists for many hours past the descent of the shear layer, at least below 25-m depth. This latter case represents observations from the highly sheared and highly stratified flow in the upper equatorial ocean (Smyth et al. 2013). Below 25 m, the shear created by the opposing South Equatorial Current and Equatorial Undercurrent is roughly in balance with the stratification to maintain Ri near a value of 1/4 (Smyth & Moum 2013). Here, a diurnal cycle in turbulence (**Figure 6e**) persists beneath the mixed layer.

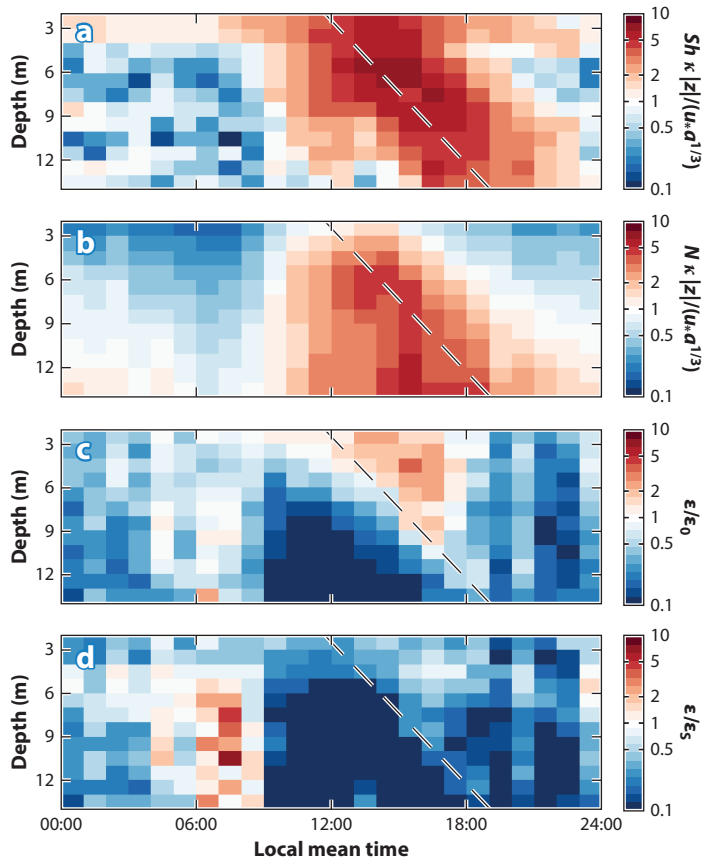


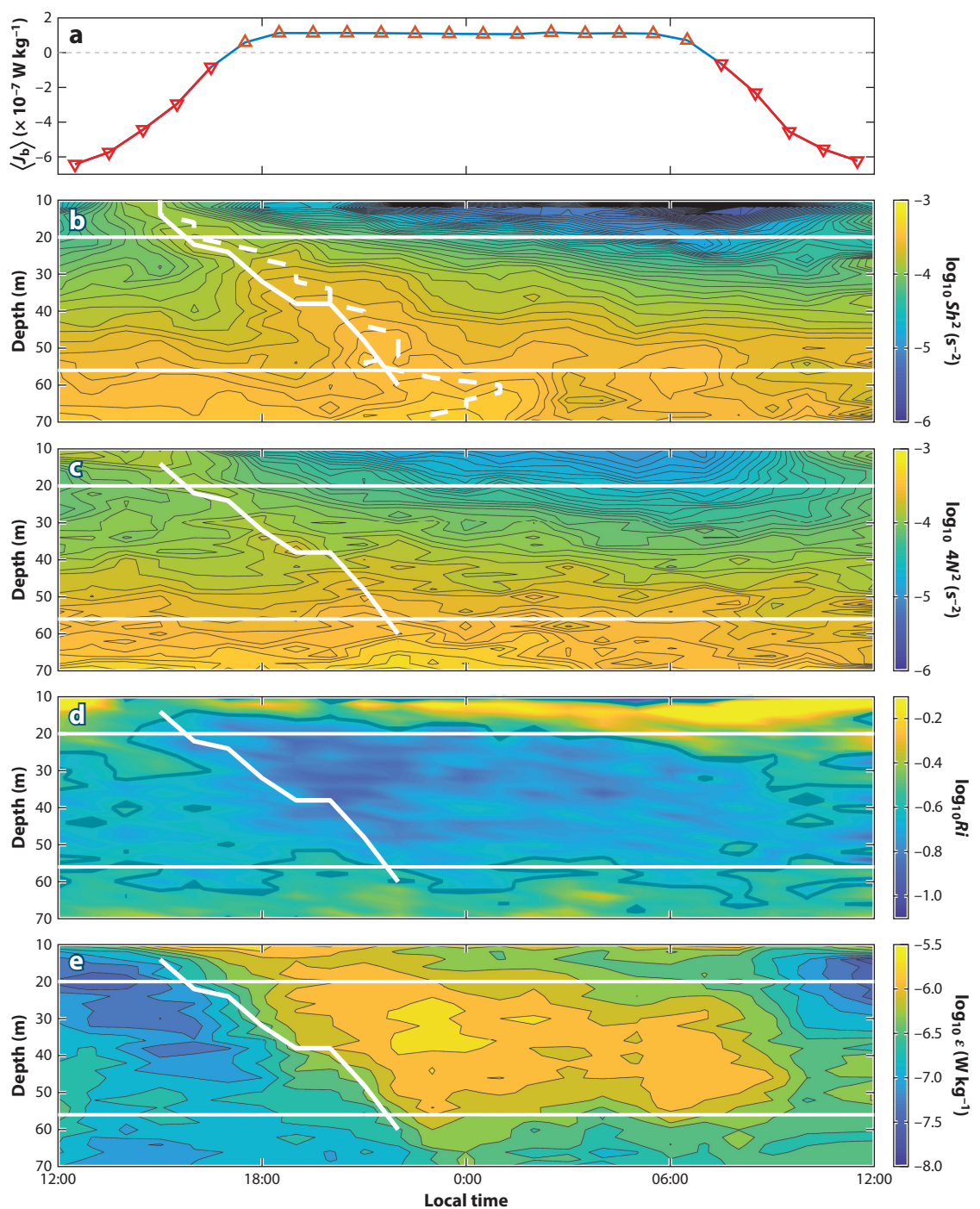
Figure 5

(*a*) Daily composite of averaged shear Sb normalized by wall-layer shear. (*b*) Daily composite of stratification N normalized by wall-layer shear. (*c,d*) Diurnally averaged ϵ normalized by two relevant parameterizations, one that includes wall-layer shear (panel *c*) and one that includes measured shear (panel *d*). The black-and-white dashed line in each panel shows the descent of the stratified base of the diurnal warm layer—here, the mean rate is 2 m h^{-1} . Figure adapted with permission from Sutherland et al. (2016).

It seems to be triggered by the deepening shear from the sea surface near the day's end in the diurnal warm layer, adding to preexisting shear below 25 m and creating shear instabilities, as in the example shown in **Figure 4**. In this case, the wind energy trapped in the diurnal warm layer is diurnally released into the upper ocean above the core of the Equatorial Undercurrent.

4.3. Tidal and Near-Inertial Periods

The tides generated by gravitational forces on the ocean by the moon and sun cause visible changes in sea level at the beach and coastal inlets. They also cause strong and often reversing currents over continental shelves and in inland seas such as the Salish Sea off western Canada and the United States. These currents generate turbulence as a consequence of the large values of Sb required so that the currents are reduced to zero at the seafloor, where particularly energetic bottom boundary layers are found (Trowbridge & Lentz 2018). Indeed, early ocean turbulence measurements in fast tidal currents of the Salish Sea produced the first clear inertial subrange spectrum of turbulence



(Caption appears on following page)

Figure 6 (Figure appears on preceding page)

Daily composite based on eight days of turbulence profiling observations on the equator. The abscissa is the local time, which lags Coordinated Universal Time by nine hours. (a) Surface buoyancy flux, J_b . (b) Squared current shear, Sb^2 . (c) Four times the squared buoyancy frequency, N^2 . (The factor of four is chosen so that Sb^2 and N^2 are the same color when Ri is near the critical value of 1/4.) (d) $Ri = N^2/Sb^2$. The dark contour represents $Ri = 1/4$. (e) ϵ . In panels b–e, the solid and dashed white curves indicate different measures of the descent rate of the shear layer. Here, the descent rate is approximately 6 m h^{-1} . Figure adapted with permission from Smyth et al. (2013).

(Grant et al. 1962), a spectrum only achieved because of the vast range of scales, from the largest permitted by the depth of the tidal channel, $\mathcal{O}(100 \text{ m})$, to the Kolmogorov scale, $\mathcal{O}(1 \text{ mm})$ —a range not available in laboratory flows that had previously failed to clarify the inertial subrange predicted by Kolmogorov (1941). Shallow seas are where most of the tidal energy is dissipated (for example, Ferrari & Wunsch 2009).

More subtly, internal waves at tidal period are generated by tidal motion in stratified oceans at topographic features (Garrett & Kunze 2007). This internal tide can cause local mixing (Polzin et al. 1997) and also propagate long distances to cause mixing hundreds or thousands of kilometers away (Nash et al. 2012). A tremendous amount of attention has been devoted to the role of this mixing in maintaining the observed deep-ocean stratification and circulation since Munk & Wunsch (1998) identified tidal energy as having a more significant role than previously thought. Numerous local experiments have been spawned (for a summary, see MacKinnon et al. 2017), and progress continues; in addition to the role played by topographically trapped waves as a mechanism for mixing (Fer et al. 2015, Fer, et al. 2016), the importance of local high-mode wave generation to tidal mixing at high latitudes has been explored through modeling and observations by Rippeth et al. (2017) and globally by Vic et al. (2019).

On continental shelves, there is a regular and important extraction of tidal energy that goes to mixing through the sharpening of the shoaling internal tide (for example, Colosi et al. 2018) and the further formation of shoreward-propagating nonlinear internal solitary-like waves that ultimately lose their energy in shallow water. The importance of this tidally driven system to coastal waters includes the induced lateral transport of mass, nutrients, plankton, and so on (Shroyer et al. 2010). Perhaps more critical to coastal ocean dynamics, these nonlinear waves cause intermittent and large diapycnal injections of heat across the base of the mixed layer, $\mathcal{O}(1 \text{ kW m}^{-2})$, as estimated from direct turbulence measurements by Moum et al. (2003). These heat injections are due to waves that are present much less than 10% of the time at a point in space. This factor is not accounted for in coastal models but may dominate mixed-layer cooling, particularly during times of weak atmospheric forcing (Shroyer et al. 2010).

The other globally ubiquitous form of internal waves, and one that may make a larger contribution to mixing than internal tides, are those with a near-inertial period (Alford et al. 2016). Wind-forced near-inertial motions in the mixed layer induce shear at its base and, via turbulence-enhanced mixing, aid in its deepening (Sanford et al. 2011). Because of their relatively small vertical scales, downward-propagating near-inertial waves create layers of high shear where mixing is elevated (Gregg et al. 1986, Hebert & Moum 1994, Alford & Gregg 2001). Parameterized mixing estimates (using profiling Argo float data; Whalen et al. 2012) roughly correlate with seasonally varying storm tracks, increasing and decreasing with a climatology of near-inertial mixed layer energy. Extreme wind forcing in the form of tropical cyclones excites near-inertial energy in the upper ocean that is considered the primary source of mixing and, in turn, contributes to the cold wake of the storm (Emanuel 2003, D’Asaro et al. 2007).

Another, and unexpected, source of near-inertial energy may come from the reflection of surface-generated and equatorially trapped waves reflecting off the seafloor (Delorme & Thomas 2019). Subsequent vertical shear is sufficient to create low Ri where mixing ensues over broad

regions above equatorial seafloors. This may explain the enhanced near-bottom equatorial mixing observed by Holmes et al. (2016) over a topographically smooth seafloor and contribute significantly to intensified diapycnal upwelling near the equator in the abyss.

4.4. Timescales Too Long for Resolution by Shipboard Measurement

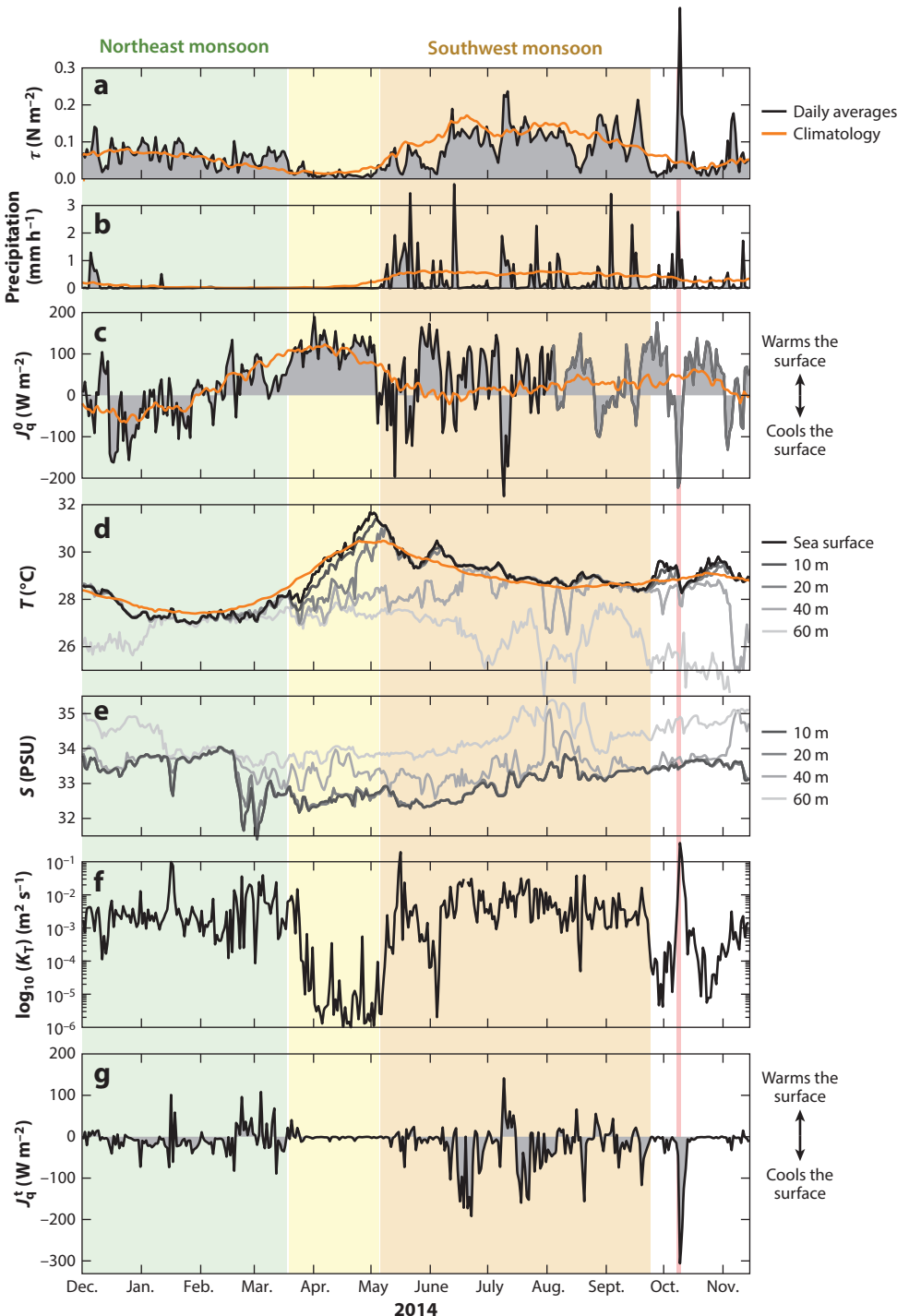
To address the important questions of temporal variations in mixing on timescales longer than a month or so, new types of measurement platforms have been developed in the past 15-plus years. These platforms have allowed long time series measurements from (so far) oceanographic moorings and autonomous gliders. One way to make turbulence measurements from gliders is with turbulence sensors mounted on the body (St. Laurent & Merrifield 2017). Another way is to infer the part of the body motion that is caused by turbulent motions on larger scales, an inference that Beaird et al. (2012) referred to as a large-eddy method and led to three years of ϵ estimates from glider observations in dense overflows of the North Atlantic.

The results summarized below illustrate how upper-ocean mixing varies on these longer timescales, and reflect variations in surface forcing that occur on these timescales but on large spatial scales that are not resolved by point measurements in the ocean.

4.4.1. Monsoonal timescales. The predictability of the South Asian monsoons is critical to the health and safety of the large populations of Indian Ocean rim countries. One of the limiting factors is proper representation of ocean mixing in models of the complex structure of the Bay of Bengal, where fresh water and temperature alternately dominate upper-ocean stratification (Goswami et al. 2016) and where turbulence measurements have been scarce. A year-long record from a single moored χ pod at 15-m depth in the central Bay of Bengal yields a view of the mixing associated with both northeast (dry) and southwest (wet) monsoons and the transition period between them (Warner et al. 2016). The variation of K_T derived from daily estimates (Figure 7) shows variability over six orders of magnitude, from near γ during the sunny and windless transition, when the upper ocean warms rapidly, to values approaching $1 \text{ m}^2 \text{ s}^{-1}$ during the passage of a building tropical storm that passed within 100 km of the mooring. Variations on turbulence-decay timescales are greater by another two orders of magnitude. Because of the stabilizing influence of fresh water on the stratification, the temperature gradient changes sign frequently, so that J_q^t alternately cools and heats the water above 15-m depth. Averaged over the northeast monsoon, the surface is cooled by the atmosphere at nearly the same rate as it is cooled from below by mixing (approximately 7 W m^{-2}). Over the rainy and windier southwest monsoon, the atmosphere heats the ocean by approximately 30 W m^{-2} , but the net effect on the mixed layer is tempered by subsurface cooling of 22 W m^{-2} . This data set demonstrates not only what can be learned from long time series measurements of mixing but also the ability to make measurements of the upper ocean under conditions far too severe for shipboard measurements, such as immediately beneath tropical cyclones.

An important factor that limits accurate mixing estimates in seas that are at least intermittently dominated by freshwater stratification is accurate and extended moored measurements of conductivity to determine salinity and its contribution to N^2 . Indian scientists are continuing to lead this effort (Venkatesan et al. 2019).

4.4.2. Seasonal timescales. Recent glider deployments in the North Atlantic (three deployments in approximately the same area over a one-year period) have provided a year-long profiling record of estimates of upper-ocean turbulence using a modified large-eddy method (Evans et al. 2018). These data show an annual cycle in mixed-layer turbulence that supports



(Caption appears on following page)

Figure 7 (Figure appears on preceding page)

Variability of upper-ocean mixing associated with the monsoons in the Bay of Bengal. Four time periods are highlighted with background shading: the northeast monsoon (December 1, 2013–March 18, 2014; green), the weak-wind and zero-precipitation transition between the northeast and southwest monsoons (March 19–May 5, 2014; yellow), the southwest monsoon (May 6–September 24, 2014; tan), and the passage of Tropical Storm Hudhud (October 8–10, 2014; red). (a) Daily averaged surface wind stress (black line and gray shading) from the RAMA mooring at 12°N, 90°E, from December 1, 2013, through November 21, 2014. (b) Daily averaged precipitation rate. (c) Atmospheric (net surface) heat flux (J_q^0). Negative values indicate heat flux out of the ocean, and positive values indicate heat flux into the ocean. (d) Sea surface temperatures (black line) and subsurface temperatures at 10 m, 20 m, 40 m, and 60 m (gray lines). In panels a–d, the orange lines show climatological averages calculated from the 1979–2015 TropFlux data product for wind stress, atmospheric heat flux, and temperature, and from the 1948–2015 National Centers for Environmental Prediction Reanalysis 1 (NCEP1) data product for precipitation. (e) Subsurface salinities at 10 m, 20 m, 40 m, and 60 m. (f) Turbulence diffusivity (K_T) as measured by a χ pod at 15-m depth. (g) Turbulent heat flux (J_q^r) at 15 m. Positive values indicate upward heat flux that warms the sea surface, and negative values indicate downward heat flux that cools the sea surface. Figure adapted from Warner et al. (2016) under a CC BY 4.0 license (<https://creativecommons.org/licenses/by/4.0/>).

existing depth-dependent scalings based on forcing of the turbulence by surface buoyancy and wind.

The first six years of the χ pod record from the NOAA mooring at 0°, 140°W, in the cold tongue of the equatorial Pacific have led to an examination of the annual signal in air-sea heat flux divergence—the difference between atmospheric heating and turbulence-enhanced subsurface cooling—in determining SST variation (Moum et al. 2013). In the equatorial cold tongues (there is a cold tongue in the Atlantic as well, although not in the Indian Ocean, due to fundamentally different large-scale wind systems), SST varies on an annual cycle, as it also does at temperate latitudes, where net surface heat flux also varies annually. However, in the tropics, the sun passes overhead twice a year, leading to a semiannual peak in net surface heat flux (Xie 2013). With an accounting for a small amount of advective heating, the dominant role of subsurface turbulence in cooling the sea surface is made clear. When heating of the surface from above exceeds cooling from below, the sea surface heats, and vice versa, as indicated in **Figure 8**. This example highlights the complementary roles of equatorial upwelling, which is modulated by the winds and brings cool water closer to the surface, and mixing, which thermodynamically modifies the temperature of fluid parcels and is a necessary component of SST modification.

4.4.3. Interannual timescales. The even longer, 11-year χ pod record at 0°, 140°W, spans a few El Niño–Southern Oscillation events. These events include examples of cooling and warming phase transitions to and from the neutral state for both El Niño and La Niña (Warner & Moum 2019). Sorting the data into these phase transitions shows that the magnitude of the air-sea heat flux divergence alone is sufficient to account for the SST cooling and warming (**Figure 9**). In this way, mixing works to strengthen the El Niño–Southern Oscillation state and must be considered part of a positive Bjerknes feedback mechanism that amplifies atmospheric teleconnections. Hence, the turbulence on timescales of seconds to minutes and length scales of centimeters to meters plays a fundamental role in global climate. While not unexpected to many, this demonstration provides a key argument for continuous monitoring of turbulence in the ocean, so that we can eventually tie together the full hierarchy of fluid motions leading to turbulence in the form of better ocean mixing parameterizations for coupled models. Other examples of feedback are noted in the sidebar titled Mixing Feeds Back to the Atmosphere.

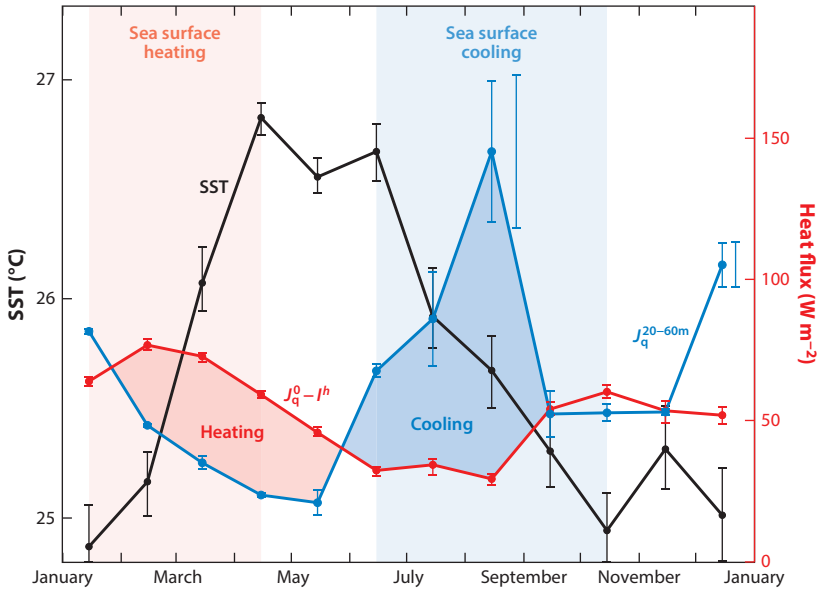


Figure 8

Sea surface temperature (SST) (black line), turbulent heat flux over a 20–60-m depth range ($J_q^{20–60m}$; blue line) and the part of the surface heat flux that contributes to mixed-layer heating ($J_q^0 - I^b$, where I^b is the solar radiation penetrating through depth b) from the TropFlux data product, showing how seasonally varying SST in the equatorial cold tongue. Natural variability is represented by 95% bootstrap confidence intervals on 15-min averages of J_q^t for the largest (August) value by the adjacent blue bar, and for all of the data by the blue bar adjacent to the December value. Figure adapted with permission from Moum et al. (2013).

5. LAMINAR OCEANS

The initial motivations to study ocean turbulence involved detecting submarine-generated turbulence. This idea was based on the rationale that only weak sources of turbulence were to be found in the ocean [this was in the 1950s, as recounted by Gregg (1991), and led ultimately to the famous measurements by Grant et al. (1962) that defined the spectrum of turbulence]. We now have a reasonably repeatable assessment of abyssal values of K_T that are, on average, approximately 100 times greater than molecular values (see, for example, figure 5 in Moum & Rippeth 2009) from measurements made at different times and different locations using very different methods. While there might be a tendency these days to think that the ocean is always and everywhere turbulent, apparently this is not true. Moored measurements at 105-m depth in the southern Bay of Bengal indicate extended periods when there is no detectable mixing (Cherian et al. 2020) (Figure 10). This is shown by the two-month period (March–May 2014) where daily averaged values of K_T are indistinguishable from γ . While surface forcing is not negligible at the beginning of this period, stratification is sufficiently strong to isolate the ocean, at least above 105 m, from surface effects. This is similar to the buoyant suppression of turbulence in the northern Bay of Bengal with the arrival of fresh water from the Brahmaputra–Ganga–Meghna delta during the rainy southwest monsoon (Thakur et al. 2019) or by heavy rain squalls anywhere (Smyth et al. 1997). Apparently, any internal motions, including waves, are not energetic enough at small scales to excite turbulence.

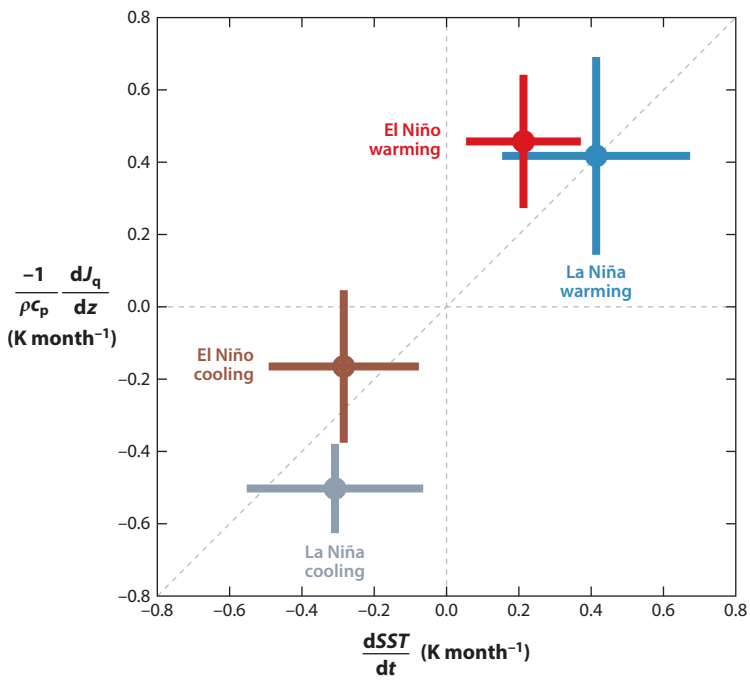


Figure 9

Observed tendency of monthly averaged sea surface temperature (SST) (abscissa) during the four El Niño–Southern Oscillation (ENSO) phase change regimes compared with the vertical heat flux divergence (ordinate). Variations in mixing on ENSO timescales account for ENSO SST warming or cooling. Figure adapted with permission from Warner & Moum (2019).

MIXING FEEDS BACK TO THE ATMOSPHERE

The mixing cycle in the cold tongues that positively feeds back to El Niño–Southern Oscillation phase change (Warner & Moum 2019) and the diurnal heating of the ocean that drives daytime convection in the marine boundary layer (Ruppert & Johnson 2016) are two examples of how mixing in the ocean affects the atmosphere. Some other examples are a little surprising:

- SST cooling by turbulence generated by wind mixing and near-inertial motions beneath tropical cyclones reduces the upper-ocean heat energy immediately available to following tropical cyclones (Emanuel 2003, Johnston et al. 2020), a negative feedback. Note that dissipative heating in tropical cyclones represents positive feedback.
- Similarly, the westerly wind bursts in the Indian Ocean and western Pacific associated with deep atmospheric convection of the 30–90-day cycle of the Madden–Julian Oscillation may reduce upper-ocean heat content sufficiently to weaken convection (and hence the Madden–Julian Oscillation) of subsequent events (Moum et al. 2016).
- Particularly intense tidal mixing in coastal seas produces fortnightly oscillations in SST. These oscillations in turn cause an atmospheric tide, observed in local air temperature and surface winds (Iwasaki et al. 2015, Ray & Susanto 2019).
- Model studies by Jochum et al. (2013) suggest that mixing by near-inertial motions in the upper ocean may be a significant contributor to tropical SST and rainfall.

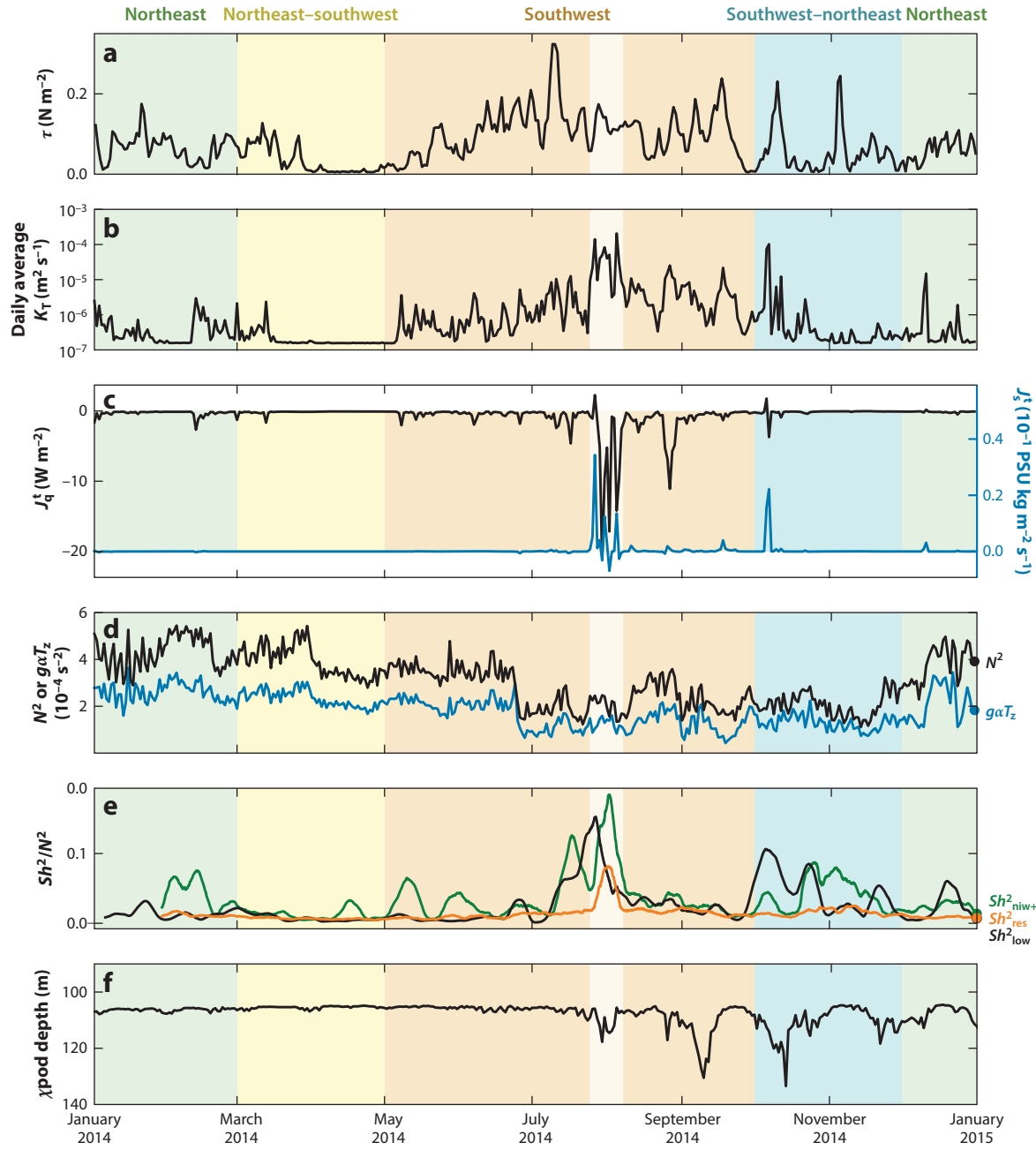


Figure 10

Extended laminar mixing regimes from a year of observations at 105-m depth and 8°N in the Bay of Bengal, showing time series of the following daily averaged quantities: (a) wind stress, τ ; (b) turbulence diffusivity, K_T ; (c) turbulent heat and salt fluxes, J_q and J_s ; (d) buoyancy frequency, N^2 , and the temperature contribution to N^2 , $N_T^2 = g\alpha T_z$; (e) weekly running mean of filtered squared shear magnitude normalized by N^2 , with low pass Sh_{low} in black, near-inertial bandpass Sh_{niw+} in green, and residual Sh_{res} in orange; and (f) χ pod depth. Background colors mark seasons. Figure adapted with permission from Cherian et al. (2020).

6. SUMMARY REMARKS

In the sense that we have only just started to obtain the types of long-term measurements of turbulence that allow an evaluation of mixing's role in processes that last longer than a shipboard campaign, this review is premature. But perhaps it will help to motivate the measurements necessary to quantify mixing rates on longer (100-year) timescales that will help to determine how and where the ocean takes up heat from the atmosphere on climate timescales.

One target for long-term turbulence measurements is the cold tongue in the equatorial Pacific, where model studies indicate that a disproportionate amount of atmospheric heat is input to the ocean (Holmes et al. 2019). Indeed, it has been suggested (with no conclusive measurement) that ocean heat uptake via mixing in the cold tongue may have been responsible for the 2000–2012 global hiatus in atmospheric warming (Held 2013, Kosaka & Xie 2013).

The IPCC's recent publication *Special Report on the Ocean and Cryosphere in a Changing Climate* (IPCC 2019) expressed concerns about increased upper-ocean stratification that could reduce mixing of heat to the deep ocean. However, an alternative scenario might feature an intensified near-surface waveguide (thermocline) along which propagate large-amplitude nonlinear internal waves that intermittently inject heat across the thermocline in a manner similar to what happens in present coastal zones (Shroyer et al. 2010). In this scenario, both measurement and prediction will be extremely challenging.

The importance of the smallest scales of motion to geophysical-scale dynamics and to global climates is now generally appreciated. But until recently, measurement of ocean turbulence/mixing/microstructure has been conducted primarily by a few experts. The greater availability of sensors and platforms has led to greater participation as well as the energetic development of new techniques. Long-term monitoring of ocean turbulence by a number of means is now an achievable goal. It is also possible that we will learn from applying simple techniques to existing operational platforms (see the sidebar titled Recommendation: Instrument More Platforms, but Simply).

RECOMMENDATION: INSTRUMENT MORE PLATFORMS, BUT SIMPLY

From a firm grounding in aeronautical engineering, Bunker (1955) demonstrated how to sense motions from aircraft accelerometer measurements that sense the buffeting of the aircraft by turbulence, or wind gusts, and use them to quantify horizontal and vertical turbulent components of the wind (65 years ago!). MacCready (1962) added small-scale turbulence sensors to his sailplane to measure the full spectrum of turbulence at scales ranging from many times larger to many times smaller than the sailplane. Much effort has been put into adding small-scale turbulence sensors to towed, profiling, and autonomous platforms. The effort by Beaird et al. (2012) to replicate Bunker's measurement on a glider ought to lead to greater application. Current microelectromechanical accelerometers are widely used in, for example, the automobile and gaming industries (and, for that matter, on χ pods). These sensors are small, inexpensive, low power, and more than sensitive enough to find greater utility on the autonomous platforms that are now in common use in the oceanographic community. An example would be Argo floats, although the development of both small-scale platform dynamics and reliable algorithms to reduce and transmit reduced data will require considerable effort.

Another approach would be to use the anisotropic turbulence scalings that generally extend to lower horizontal than vertical wavenumbers in the inertial–convective subrange of both velocity (Moum 2015) and scalar (Zhang & Moum 2010) spectra. The sampling requirements are less restrictive, meaning that relatively slowly responding sensors can be employed and data storage requirements are reduced. A cautionary note with this approach is that estimates of ϵ and χ from isotropic scalings at high wavenumber do not always agree (Becherer & Moum 2017), and we do not yet know why.

DISCLOSURE STATEMENT

The author is not aware of any affiliations, memberships, funding, or financial holdings that might be perceived as affecting the objectivity of this review.

ACKNOWLEDGMENTS

The author appreciates the great comments and suggestions on an early draft provided by colleagues Johannes Becherer, Deepak Cherian, Bertrand Delorme, Simon DeSzoek, Ken Hughes, Dick Johnson, Aurélie Moulin, Emily Shroyer, Bill Smyth, Leif Thomas, and Sally Warner. He also acknowledges the many years of support provided by the National Science Foundation and the Office of Naval Research.

LITERATURE CITED

- Alford MH, Gregg MC. 2001. Near-inertial mixing: modulation of shear, strain and microstructure at low latitude. *J. Geophys. Res.* 106:16947–68
- Alford MH, MacKinnon JA, Simmons HL, Nash JD. 2016. Near-inertial internal gravity waves in the ocean. *Annu. Rev. Mar. Sci.* 8:95–123
- Anis A, Moum JN. 1992. The superadiabatic surface layer of the ocean during convection. *J. Phys. Oceanogr.* 22:1221–27
- Anis A, Moum JN. 1994. Prescriptions for heat flux and entrainment rates in the upper ocean during convection. *J. Phys. Oceanogr.* 24:2142–55
- Beaird N, Fer I, Rhines P, Eriksen C. 2012. Dissipation of turbulent kinetic energy inferred from Seagliders: an application to the eastern Nordic Seas overflows. *J. Phys. Oceanogr.* 42:2268–82
- Becherer J, Moum JN. 2017. An efficient scheme for onboard reduction of moored xpod data. *J. Atmos. Ocean. Technol.* 34:2533–46
- Bird RB, Stewart WE, Lightfoot EN. 2007. *Transport Phenomena*. New York: Wiley. 2nd ed.
- Bister M, Emanuel KA. 1998. Dissipative heating and hurricane intensity. *Meteorol. Atmos. Phys.* 65:233–40
- Brainerd KE, Gregg MC. 1993. Diurnal restratification and turbulence in the oceanic surface mixed layer: 2. Modeling. *J. Geophys. Res.* 98:22657–64
- Brubaker JM. 1987. Similarity structure in the convective boundary layer of a lake. *Nature* 330:742–45
- Bunker AF. 1955. Turbulence and shearing stresses measured over the North Atlantic Ocean by an airplane acceleration technique. *J. Meteorol.* 12:445–55
- Chang M-H, Jheng S-Y, Lien R-C. 2016. Trains of large Kelvin-Helmholtz billows observed in the Kuroshio above a seamount. *Geophys. Res. Lett.* 43:8654–61
- Cherian DA, Shroyer EL, Wijesekera H, Moum JN. 2020. The seasonal cycle of upper-ocean mixing at 8°N in the Bay of Bengal. *J. Phys. Oceanogr.* 50:323–42
- Colosi JA, Kumar N, Suanda SH, Freismuth TM, MacMahan JH. 2018. Statistics of internal tide bores and internal solitary waves observed on the inner continental shelf off Point Sal, California. *J. Phys. Oceanogr.* 48:123–43
- D’Asaro EA, Lien R-C. 2007. Lagrangian measurements of waves and turbulence in stratified flows. *J. Phys. Oceanogr.* 30:641–55
- D’Asaro EA, Sanford TB, Niiler PP, Terrill EJ. 2000. Cold wake of Hurricane Frances. *Geophys. Res. Lett.* 34:L15609
- Delorme BL, Thomas LN. 2019. Abyssal mixing through critical reflection of equatorially trapped waves off smooth topography. *J. Phys. Oceanogr.* 49:519–42
- DeSzoek SP, Edson JB, Marion JR, Fairall CW, Bariteau L. 2015. The MJO and air-sea interaction in TOGA COARE and DYNAMO. *J. Clim.* 28:597–622
- Dillon TM, Caldwell DR. 1980. The Batchelor spectrum and dissipation in the upper ocean. *J. Geophys. Res.* 85:1910–16

- Emanuel K. 2003. Tropical cyclones. *Annu. Rev. Earth Planet. Sci.* 31:75–104
- Evans DG, Lucas NS, Hemsley VS, Frajka-Williams E, Naveira Garabato AC, et al. 2018. Annual cycle of turbulent dissipation estimated from Seagliders. *Geophys. Res. Lett.* 45:10560–69
- Fairall CW, Bradley EF, Godfrey JS, Wick GA, Edson JB, Young GS. 1996. Cool-skin and warm-layer effects on sea surface temperature. *J. Geophys. Res.* 101:1295–308
- Fer I, Muller M, Peterson AK. 2015. Tidal forcing, energetics, and mixing near the Yermak Plateau. *Ocean Sci.* 11:287–304
- Fer I, Muller M, Peterson AK. 2016. Observations of energetic turbulence on the Weddell Sea continental slope. *Geophys. Res. Lett.* 43:760–66
- Ferrari R, Wunsch C. 2009. Ocean circulation kinetic energy: reservoirs, sources, and sinks. *Annu. Rev. Fluid Mech.* 41:253–82
- Gargett AE. 1994. Observing turbulence with a modified acoustic Doppler current profiler. *J. Ocean. Atmos. Technol.* 11:1592–610
- Gargett AE, Osborn TR, Nasmyth PW. 1984. Local isotropy and the decay of turbulence in a stratified fluid. *J. Fluid Mech.* 144:231–80
- Garrett C, Kunze E. 2007. Internal tide generation in the deep ocean. *Annu. Rev. Fluid Mech.* 39:57–87
- Geyer WR, Lavery A, Scully ME, Trowbridge JH. 2010. Mixing by shear instability at high Reynolds number. *Geophys. Res. Lett.* 37:L22607
- Goswami BN, Rao SA, Sengupta D, Chakravorty S. 2016. Monsoons to mixing in the Bay of Bengal: multiscale air-sea interactions and monsoon predictability. *Oceanography* 29(2):18–27
- Grant HL, Stewart RW, Moilliet A. 1962. Turbulence spectra from a tidal channel. *J. Fluid Mech.* 12:241–68
- Gregg MC. 1977. Variations in the intensity of small-scale mixing in the main thermocline. *J. Phys. Oceanogr.* 7:436–54
- Gregg MC. 1991. The study of mixing in the ocean: a brief history. *Oceanography* 4(1):39–45
- Gregg MC, D'Asaro EA, Riley JJ, Kunze E. 2018. Mixing efficiency in the ocean. *Annu. Rev. Mar. Sci.* 10:443–73
- Gregg MC, D'Asaro EA, Shay TJ, Larson N. 1986. Observations of persistent mixing and near-inertial internal waves. *J. Phys. Oceanogr.* 16:856–85
- Hebert D, Moum JN. 1994. Decay of a near-inertial wave. *J. Phys. Oceanogr.* 24:2334–51
- Held I. 2013. The cause of the pause. *Nature* 501:318–19
- Holmes RN, Moum JN, Thomas LN. 2016. Evidence for seafloor-intensified mixing by surface-generated equatorial waves. *Geophys. Res. Lett.* 43:1202–10
- Holmes RN, Zika JD, England MH. 2019. Diathermal heat transport in a global ocean model. *J. Phys. Oceanogr.* 49:141–61
- Hughes KG, Moum JN, Shroyer EL. 2020. Evolution of the velocity structure in the diurnal warm layer. *J. Phys. Oceanogr.* 50:615–31
- Imberger J. 1985. The diurnal mixed layer. *Limnol. Oceanogr.* 30:737–70
- IPCC (Intergov. Panel Clim. Change). 2019. *Special report on the ocean and cryosphere in a changing climate*. Rep., IPCC, Geneva. <https://www.ipcc.ch/srocc>
- Iwasaki S, Isobe A, Miyao Y. 2015. Fortnightly atmospheric tides forced by spring and neap tides in coastal waters. *Sci. Rep.* 5:10167
- Jochum M, Briegleb BP, Danabasoglu G, Large WG, Jayne SR, et al. 2013. On the impact of oceanic near-inertial waves on climate. *J. Clim.* 26:2833–44
- Johnston TMS, Rudnick DL, Brizuela N, Moum JN. 2020. Advection by the North Equatorial Current of a cold wake due to multiple typhoons in the western Pacific: measurements from a profiling float array. *J. Geophys. Res.* 125:e2019JC015534
- Klymak JM, Gregg MC. 2004. Tidally generated turbulence over the Knight Inlet sill. *J. Phys. Oceanogr.* 34:1135–51
- Kolmogorov AN. 1941. Local structure of turbulence in an incompressible viscous fluid at very large Reynolds numbers. *Dokl. Akad. Nauk SSSR* 30:299–301
- Kosaka Y, Xie SP. 2013. Recent global warming hiatus tied to equatorial Pacific surface cooling. *Nature* 501:403–7

- Kunze E. 2019. A unified model spectrum for anisotropic stratified and isotropic turbulence in the ocean and atmosphere. *J. Phys. Oceanogr.* 49:385–407
- Ledwell J, Duda T, Sundermeyer M, Seim H. 2004. Mixing in a coastal environment: 1. A view from dye dispersion. *J. Geophys. Res.* 109:C10013
- Ledwell J, St. Laurent LC, Girton J, Toole J. 2011. Diapycnal mixing in the Antarctic Circumpolar Current. *J. Phys. Oceanogr.* 41:241–46
- Ledwell J, Montgomery E, Polzin K, St. Laurent LC, Schmitt R, Toole J. 2000. Evidence for enhanced mixing over rough topography in the abyssal ocean. *Nature* 403:17–82
- Ledwell J, Watson A, Law C. 1998. Mixing of a tracer in the pycnocline. *J. Geophys. Res.* 103:2149–529
- Lindborg E. 2006. The energy cascade in a strongly stratified fluid. *J. Fluid Mech.* 550:207–42
- Lueck RG, Wolk F, Yamazaki H. 2002. Oceanic velocity microstructure measurements in the 20th century. *J. Oceanogr.* 58:153–74
- MacCready PB. 1962. Turbulence measurements by sailplane. *J. Geophys. Res.* 67:1041–50
- MacKinnon JA, Zhao Z, Whalen CB, Waterhouse AF, Trossman DS, et al. 2017. Climate process team on internal wave-driven ocean mixing. *Bull. Am. Meteorol. Soc.* 98:2429–54
- Mashayek A, Ferrari R, Merrifield S, Ledwell JR, St. Laurent L, Naveira Garabato A. 2017. Topographic enhancement of vertical turbulent mixing in the Southern Ocean. *Nat. Commun.* 8:14197
- Moulin AJ, Moum JN, Shroyer EL. 2018. Evolution of turbulence in the diurnal warm layer. *J. Phys. Oceanogr.* 48:383–96
- Moum JN. 1996. Energy-containing scales of turbulence in the ocean thermocline. *J. Geophys. Res.* 101:14095–109
- Moum JN. 2015. Ocean speed and turbulence measurements using pitot-static tubes on moorings. *J. Atmos. Ocean. Technol.* 32:1400–13
- Moum JN, Caldwell DR, Nash JD, Gunderson GD. 2002. Observations of boundary mixing over the continental slope. *J. Phys. Oceanogr.* 32:2113–30
- Moum JN, Farmer DM, Smyth WD, Armi L, Vagle S. 2003. Structure and generation of turbulence at interfaces strained by internal solitary waves propagating shoreward over the continental shelf. *J. Phys. Oceanogr.* 33:2093–112
- Moum JN, Gregg MC, Lien RC, Carr ME. 1995. Comparison of turbulent kinetic energy dissipation rates from two ocean microstructure profilers. *J. Atmos. Ocean. Technol.* 12:346–66
- Moum JN, Lien RC, Perlin A, Nash JD, Gregg MC, Wiles PJ. 2009. Sea surface cooling at the equator by subsurface mixing in tropical instability waves. *Nat. Geosci.* 2:761–65
- Moum JN, Nash JD. 2009. Mixing measurements on an equatorial ocean mooring. *J. Atmos. Ocean. Technol.* 26:317–36
- Moum JN, Nash JD, Smyth WD. 2011. Narrowband high-frequency oscillations at the equator. Part I: interpretation as shear instabilities. *J. Phys. Oceanogr.* 41:397–411
- Moum JN, Osborn TR. 1986. Mixing in the main thermocline. *J. Phys. Oceanogr.* 16:1250–59
- Moum JN, Perlin A, Nash JD, McPhaden MJ. 2013. Seasonal sea surface cooling in the equatorial Pacific cold tongue controlled by ocean mixing. *Nature* 500:64–67
- Moum JN, Pujiana K, Lien RC, Smyth WD. 2016. Ocean feedback to pulses of the Madden–Julian Oscillation in the equatorial Indian Ocean. *Nat. Commun.* 7:13203
- Moum JN, Rippeth TP. 2009. Do observations adequately resolve the natural variability of oceanic turbulence? *J. Mar. Syst.* 77:409–17
- Munk W, Wunsch C. 1998. Abyssal recipes II: energetics of tidal and wind mixing. *Deep-Sea Res. I* 45:1977–2010
- Nash JD, Kelly SM, Shroyer EL, Moum JN, Duda TF. 2012. The unpredictable nature of internal tides on the continental shelf. *J. Phys. Oceanogr.* 41:1981–2000
- Nash JD, Moum JN. 2001. Internal hydraulic flows on the continental shelf: high drag states over a small bank. *J. Geophys. Res.* 106:4593–612
- Osborn TR. 1974. Vertical profiling of velocity microstructure. *J. Phys. Oceanogr.* 4:109–15
- Osborn TR. 1980. Estimates of the local rate of vertical diffusion from dissipation measurements. *J. Phys. Oceanogr.* 10:83–89

- Osborn TR, Cox CS. 1972. Oceanic fine structure. *Geophys. Fluid Dyn.* 3:321–45
- Perlin A, Moum JN. 2012. Comparison of thermal variance dissipation rates from moored and profiling instruments at the equator. *J. Atmos. Ocean. Technol.* 29:1347–62
- Perlin A, Moum JN, Klymak JM, Levine MD, Boyd T, Kosro PM. 2005. A modified law of the wall applied to oceanic bottom boundary layers. *J. Geophys. Res.* 110:C10S10
- Peters H, Gregg MC, Sanford TB. 1995. Details and scaling of turbulent overturns in the Pacific Equatorial Undercurrent. *J. Geophys. Res.* 100:805–45
- Polzin KL, Speer KG, Toole JM, Schmitt RW. 1996. Intense mixing of Antarctic Bottom Water in the equatorial Atlantic Ocean. *Nature* 380:54–57
- Polzin KL, Toole JM, Ledwell J, Schmitt RW. 1997. Spatial variability of turbulent mixing in the abyssal ocean. *Science* 276:93–96
- Pomeau Y. 2016. The long and winding road. *Nat. Phys.* 12:198–99
- Pope SB. 2000. *Turbulent Flows*. Cambridge, UK: Cambridge Univ. Press
- Price JF, Weller RA, Pinkel R. 1986. Diurnal cycling: observations and models of the upper ocean response to diurnal heating, cooling, and wind mixing. *J. Geophys. Res.* 91:8411–27
- Pujiana K, Moum JN, Smyth WD. 2018. The role of turbulence in redistributing upper-ocean heat, freshwater, and momentum in response to the MJO in the equatorial Indian Ocean. *J. Phys. Oceanogr.* 48:197–220
- Rainville L, Gobat J, Lee CM, Shilling GB. 2017. Multi-month dissipation estimates using microstructure from autonomous underwater gliders. *Oceanography* 30(2):49–50
- Ray RD, Susanto RD. 2019. A fortnightly atmospheric tide at Bali caused by oceanic tidal mixing in Lombok Strait. *Geosci. Lett.* 6:6
- Rippeth TP, Vlasenko V, Stashchuk N, Scannell BD, Green JAM, et al. 2017. Tidal conversion and mixing poleward of the critical latitude (an Arctic case study). *Geophys. Res. Lett.* 44:12349–57
- Roemmich D, Alford MH, Claustre H, Johnson K, King B, et al. 2019. On the future of Argo: a global, full-depth, multi-disciplinary array. *Front. Mar. Sci.* 6:439
- Ruppert JH, Johnson RH. 2016. On the cumulus diurnal cycle over the tropical warm pool. *J. Adv. Model. Earth Syst.* 8:669–90
- Sanford TB, Price JF, Girton JB. 2011. Upper ocean response to Hurricane Francis (2004) observed by profiling EM-APEX floats. *J. Phys. Oceanogr.* 41:1041–56
- Schultze LKP, Merckelbach L, Carpenter JR. 2017. Turbulence and mixing in a shallow stratified shelf sea from underwater gliders. *J. Geophys. Res.* 122:9092–109
- Shay TJ, Gregg MC. 1986. Convectively driven turbulent mixing in the upper ocean. *J. Phys. Oceanogr.* 16:1777–98
- Shroyer EL, Moum JN, Nash JD. 2010. Vertical heat flux and lateral mass transport in nonlinear internal waves. *Geophys. Res. Lett.* 37:L08601
- Shroyer EL, Rudnick DL, Farrar JT, Lim B, Venayagamoorthy SK, et al. 2016. Modification of upper-ocean temperature structure by subsurface mixing in the presence of strong salinity stratification. *Oceanography* 29(2):62–71
- Sinhaber M, Bodenschatz E, Bewley GP. 2015. Decay of turbulence at high Reynolds numbers. *Phys. Rev. Lett.* 114:034501
- Sinnet G, Feddersen F. 2018. The competing effects of breaking waves on surfzone heat fluxes: albedo versus wave heating. *J. Geophys. Res.* 123:7172–84
- Smyth WD, Carpenter JR. 2019. *Instability in Geophysical Flows*. Cambridge, UK: Cambridge Univ. Press
- Smyth WD, Moum JN. 2012. Ocean mixing by Kelvin-Helmholtz instability. *Oceanography* 25(2):140–49
- Smyth WD, Moum JN. 2013. Marginal instability and deep cycle mixing in the eastern equatorial Pacific Ocean. *Geophys. Res. Lett.* 40:6181–85
- Smyth WD, Moum JN, Caldwell DR. 2001. The efficiency of mixing in turbulent patches: inferences from direct simulations and microstructure observations. *J. Phys. Oceanogr.* 31:1969–92
- Smyth WD, Moum JN, Li L, Thorpe SA. 2013. Diurnal shear instability, the descent of the surface shear layer, and the deep cycle of equatorial turbulence. *J. Phys. Oceanogr.* 43:2432–55
- Smyth WD, Moum JN, Nash JD. 2011. Narrowband, high-frequency oscillations at the equator. Part II: properties of shear instabilities. *J. Phys. Oceanogr.* 41:412–28

- Smyth WD, Zavialov P, Moum JN. 1997. Decay of turbulence in the upper ocean following sudden isolation from surface forcing. *J. Phys. Oceanogr.* 27:810–22
- Sreenivasan KR. 1991. Fractals and multifractals in turbulence. *Annu. Rev. Fluid Mech.* 23:539–600
- St. Laurent L, Merrifield S. 2017. Measurements of near-surface turbulence and mixing from autonomous ocean gliders. *Oceanography* 30(2):116–25
- Sutherland GL, Marie L, Reverdin G, Christensen KH, Brostrom G, Ward B. 2016. Enhanced turbulence associated with the diurnal jet in the ocean surface boundary layer. *J. Phys. Oceanogr.* 46:3051–67
- Sutherland P, Melville WK. 2015. Field measurements of surface and near-surface turbulence in the presence of breaking waves. *J. Phys. Oceanogr.* 45:943–65
- Taylor JR, Marie L, de Bruyn Kops SM, Caulfield CP, Linden PF. 2019. Testing the assumptions underlying ocean mixing methodologies using direct numerical simulations. *J. Phys. Oceanogr.* 49:2761–79
- ten Doeschate A, Sutherland G, Esters L, Wain D, Walesby K, Ward B. 2017. ASIP: profiling the upper ocean. *Oceanography* 30(2):33–35
- Thakur R, Shroyer EL, Govindarajan R, Farrar JT, Weller RA, Moum JN. 2019. Seasonality and buoyancy suppression of turbulence in the Bay of Bengal. *Geophys. Res. Lett.* 46:4346–55
- Thompson EJ, Moum JN, Rutledge SA, Fairall CW. 2019. Wind limits on rain layers and diurnal warm layers. *J. Geophys. Res.* 124:897–924
- Thorpe SA. 1971. Experiments on the instability of stratified shear flows: miscible fluids. *J. Fluid Mech.* 46:299–319
- Toole JM, Polzin KL, Schmitt RW. 1994. Estimates of diapycnal mixing in the abyssal ocean. *Science* 264:1120–23
- Trowbridge JH, Lentz SJ. 2018. The bottom boundary layer. *Annu. Rev. Mar. Sci.* 10:397–420
- van Haren H, Gostiaux L. 2010. A deep-ocean Kelvin-Helmholtz billow train. *Geophys. Res. Lett.* 37:L03605
- Venkatesan R, Ramesh K, Muthiah MA, Thirumurugan K, Atmanand MA. 2019. Analysis of drift characteristic in conductivity and temperature sensors used in moored buoy system. *Ocean Eng.* 171:151–56
- Vic C, Naveira Garabato AC, Green JAM, Waterhouse AF, Zhao Z, et al. 2019. Deep-ocean mixing driven by small-scale internal tides. *Nat. Commun.* 10:2099
- Warner SJ, Becherer J, Pujiana K, Shroyer EL, Ravichandran M, et al. 2016. Monsoon mixing cycles in the Bay of Bengal: a year-long subsurface mixing record. *Oceanography* 29(2):158–69
- Warner SJ, Moum JN. 2019. Feedback of mixing to ENSO phase change. *Geophys. Res. Lett.* 46:13920–27
- Wesson JC, Gregg MC. 1994. Mixing at Camarinal Sill in the Strait of Gibraltar. *J. Geophys. Res.* 99:9847–78
- Whalen CB, Talley LD, MacKinnon JA. 2012. Spatial and temporal variability of global ocean mixing inferred from Argo profiles. *Geophys. Res. Lett.* 39:L18612
- Woods JD. 1968. Wave-induced shear instability in the summer thermocline. *J. Fluid Mech.* 32:791–800
- Wyngaard JC, Cote OR, Izumi Y. 1971. Local free convection, similarity and the budgets of shear stress and heat flux. *J. Atmos. Sci.* 28:1171–82
- Xie SP. 2013. Unequal equinoxes. *Nature* 500:33–34
- Zhang Y, Moum JN. 2010. Inertial-convective subrange estimates of thermal variance dissipation rate from moored temperature measurements. *J. Atmos. Ocean. Technol.* 27:1950–59